




# Achieved high energy density and excellent thermal stability in $(1-x)(\text{Bi}_{0.5}\text{Na}_{0.5})_{0.94}\text{Ba}_{0.06}\text{TiO}_3-x\text{Bi}(\text{Mg}_{0.5}\text{Ti}_{0.5})\text{O}_3$ relaxor ferroelectric thin films

Hao Yan<sup>1</sup>, Baijie Song<sup>1</sup>, Kun Zhu<sup>1</sup>, Liuxue Xu<sup>1</sup>, Bo Shen<sup>1\*</sup> , and Jiwei Zhai<sup>1,\*</sup>

<sup>1</sup>Key Laboratory of Advanced Civil Engineering Materials of Ministry of Education, Functional Materials Research Laboratory, School of Materials Science and Engineering, Tongji University, Shanghai 201804, China

Received: 18 February 2021

Accepted: 11 May 2021

Published online:  
25 May 2021

© The Author(s), under exclusive licence to Springer Science+Business Media, LLC, part of Springer Nature 2021

## ABSTRACT

In this work, lead-free  $(1-x)(\text{Bi}_{0.5}\text{Na}_{0.5})_{0.94}\text{Ba}_{0.06}\text{TiO}_3-x\text{Bi}(\text{Mg}_{0.5}\text{Ti}_{0.5})\text{O}_3$  (abbreviated as BNBT- $x$ BMT,  $x = 0.3, 0.4, 0.5$  and  $0.6$ ) thin films were prepared on Pt/Ti/SiO<sub>2</sub>/Si substrates using sol-gel method. The microstructures, dielectric, and energy storage properties were investigated. The results showed that the addition of BMT disrupted the long-range ferroelectric order and enhanced the relaxor behavior of BNBT- $x$ BMT thin films. In addition, the leakage current density of thin films was also reduced by the doping of a moderate amount of BMT. A high recoverable energy density of 34.36 J/cm<sup>3</sup> with an efficiency of 56.63% was achieved in the BNBT-0.5BMT thin film under the electric field of 2149 kV/cm. Furthermore, BNBT-0.5BMT thin film exhibited superior stability in the temperature range of 30 °C–145 °C and frequency range of 500 Hz–5 kHz, as well as long-term fatigue durability after  $1 \times 10^5$  cycles. These results suggest that BNBT-0.5BMT thin film may be a promising material for lead-free dielectric energy storage applications.

## 1 Introduction

The development of new energy power generation technologies places high demands on devices that efficiently store, absorb, and supply electricity [1–3]. Dielectric capacitors play an essential role in high power applications, including pulsed power systems, hybrid vehicles, and medical defibrillators, owing to their fast charge/discharge rate, high power density,

and long lifetime [4–9]. Currently, commercial dielectric capacitor materials such as biaxially oriented polypropylene (BOPP) and polyvinylidene fluoride (PVDF) generally possess relatively low melting points, limiting their application at high temperatures (> 150 °C) [10, 11]. Although polymers can be composited with inorganic materials such as ceramics to improve the comprehensive energy storage performance of the material, the low energy

Address correspondence to E-mail: shenbo@tongji.edu.cn; apzhai@tongji.edu.cn

density is a bottleneck for miniaturization [12, 13]. In contrast, inorganic dielectric thin film capacitors not only have high energy density but also exhibit excellent stability over a wide range of operating temperatures, which enables them to meet the requirements of power electronics in extreme operating environments [14, 15].

In general, the total energy density ( $W$ ), recoverable energy density ( $W_{rec}$ ), and efficiency ( $\eta$ ) of the dielectric capacitor can be calculated from the polarization–electric field hysteresis ( $P$ – $E$ ) loops:

$$W = \int_0^{P_{max}} EdP \quad (1)$$

$$W_{rec} = \int_{P_r}^{P_{max}} EdP \quad (2)$$

$$\eta = \frac{W_{rec}}{W} \times 100\% \quad (3)$$

where  $E$  is the applied electric field,  $P$  is the polarization,  $P_{max}$  is the maximum polarization, and  $P_r$  is the remnant polarization. Therefore, large polarization, high dielectric breakdown strength (BDS), and small hysteresis are the keys to ensure high energy storage density, and efficiency. Relaxor ferroelectrics (RFEs) are characterized by slender hysteresis loops with high polarization and small remnant polarization, which are conducive to efficient energy storage. The lead-containing RFEs solid solutions such as  $Pb(Mg_{1/3}Nb_{2/3})O_3$  (PMN) and  $Pb(Zn_{1/3}Nb_{2/3})O_3$  (PZN) [16] and  $BiMeO_3$ – $PbTiO_3$  (Me is a single cation or a combination of average trivalent mixed cations) [17] may cause irreversible harm to the ecosystem, thus research on lead-free energy storage dielectrics is imperative. Sodium bismuth titanate (BNT) is an ideal alternative to lead-containing materials as the  $Bi^{3+}$  ion possesses a lone pair electron  $6s^2$  conformation similar to that of the  $Pb^{2+}$  ion, which can hybridize with O  $2p$  orbitals, leading to high saturation polarization [18, 19]. However, BNT exhibits strong ferroelectricity with square hysteresis loops at room temperature, resulting in considerable energy dissipation. For BNT, RFEs are accessible by chemical modifications at room temperature. Thus, a number of perovskite compounds, for instance,  $BaTiO_3$  [20],  $Bi_{0.5}K_{0.5}TiO_3$  [21],  $SrTiO_3$  [22],  $NaNbO_3$  [23] are combined with BNT to form RFEs to reduce the polarization hysteresis and improve the energy storage density and efficiency [24].

Enlarging  $\Delta P$  ( $P_{max} - P_r$ ) and improving BDS of the material are the two mainstream paths to enhance the

$W_{rec}$ . Several research reports indicate that the oxygen octahedron tilts to pseudocubic symmetry when the tolerance factor decreases, which is beneficial to the phase transition from ferroelectric to relaxor [25, 26]. For instance, Sun et al. obtained a large  $\Delta P$  of  $78.47 \mu C/cm^2$  and an excellent recoverable energy density ( $W_{rec}$ ) of  $40.8 J/cm^3$  under the electric field of  $1500 kV/cm$  in  $0.5(Bi_{0.5}Na_{0.5})TiO_3 - 0.5Bi(Zn_{0.5}Zr_{0.5})O_3$  relaxor ferroelectric thin film via microstructural engineering [27]. However, the high leakage current density arising from the evaporation of Bi and Na elements during the preparation of thin films plays a negative role in enhancing the BDS of the thin films [28]. According to Zhang [29], moderate oxygen vacancies can serve as trap sites to deepen the electron trap energy level and improve the BDS. When the  $Ti^{4+}$  ions are substituted by cations with a larger radius in the lower valence state, the introduced partial oxygen vacancies are expected to facilitate the improvement of the BDS of the thin films. In addition, the lattice compressive stress caused by the large ion substitution flattens the free energy distribution, thereby favoring an increase in the maximum polarization [29, 30].

In this work, we chose the solid solution of  $0.94Bi_{0.5}Na_{0.5}TiO_3 - 0.06BaTiO_3$  (BNBT) as the basic material, since this component is located near the morphotropic phase boundary (MPB). Moreover,  $Bi(Mg_{0.5}Ti_{0.5})O_3$  was selected as the third component to improve the polarization and insulating properties of the thin films. The  $(1-x)(Bi_{0.5}Na_{0.5})_{0.94}Ba_{0.06}TiO_3 - xBi(Mg_{0.5}Ti_{0.5})O_3$  ( $x = 0.3, 0.4, 0.5$  and  $0.6$ ) lead-free relaxor ferroelectric thin films were prepared by the sol–gel method. The microstructure, dielectric properties, energy storage energy properties, frequency stability, thermal stability, and long-term fatigue resistance of BNBT- $x$ BMT thin films were systematically investigated.

## 2 Experimental procedure

The  $(1-x)(Bi_{0.5}Na_{0.5})_{0.94}Ba_{0.06}TiO_3 - xBi(Mg_{0.5}Ti_{0.5})O_3$  ( $x = 0.3, 0.4, 0.5$  and  $0.6$ ) thin films were deposited on Pt(111)/Ti/SiO<sub>2</sub>/Si substrates via sol–gel method. The sol–gel method is simple to operate and allows good control of the stoichiometric ratio of the product, so it is suitable for the preparation of thin film materials [31, 32]. For the preparation of BNBT- $x$ BMT precursor solution, sodium acetate trihydrate,

bismuth nitrate pentahydrate, barium acetate, magnesium acetate tetrahydrate, and tetrabutyl titanate were employed as raw materials. Acetic acid and 2-methoxyethanol were used as solvents and appropriate amounts of acetylacetone were added as stabilizing additives. An additional 10% excess of bismuth nitrate was added to compensate for the loss of bismuth during the high-temperature treatment. In the first step, sodium acetate trihydrate, bismuth nitrate pentahydrate, barium acetate, and magnesium acetate tetrahydrate were dissolved into acetic acid and stirred at 70 °C for 30 min. In the second step, tetrabutyl titanate was mixed with acetylacetone and 2-methoxyethanol and stirred for 30 min. Subsequently, the two solutions were mixed and stirred at 50 °C for 5 h, and then aged for 48 h. The concentration of the final precursor solution was adapted to 0.25 M. Afterwards, the prepared precursor solution was spin-coated at 3000 rpm for 30 s on Pt(111)/Ti/SiO<sub>2</sub>/Si substrates. After coating, the wet layer was treated at 200 °C, 450 °C, and 700 °C for 5 min for each. The spin-coating and heat treatment steps were repeated to obtain the desired thickness. Finally, the thin films were annealed in air at 700 °C for 30 min to crystallize.

The crystal structure of the samples was characterized by an X-ray diffractometer (XRD, D/Max 2550 V, Rigaku, Cu K<sub>α</sub> radiation, Japan). The micro-morphology of the thin films was observed by field emission scanning electron microscopy (FESEM, S-4700, HITACHI, Japan). Gold top electrodes (0.3 mm in diameter) were sputtered onto the thin films to test the dielectric properties. The polarization–electric field (*P*–*E*) hysteresis loops were measured with the ferroelectric test system (Radiant Precision Premier II). The dielectric properties were determined using a precision LCR meter (E4980A Agilent Inc., USA). Piezoelectric response force microscopy (PFM) was used to examine the local domain structure of the thin films.

### 3 Results and discussion

The XRD patterns of BNBT-*x*BMT (*x* = 0.3, 0.4, 0.5 and 0.6) thin films with the 2θ range from 20 to 60° are shown in Fig. 1a. All the compositions are polycrystalline structures with random orientation and show perovskite-dominated phase structure, indicating the formation of BNBT-*x*BMT solid solutions.

In addition, a diffraction peak of 2θ ≈ 33° is detected in the BNBT-0.5BMT thin film, which corresponds to the K<sub>α</sub> diffraction peak of (200) planes of Si [33]. Figure 1b exhibits the amplified (110) peaks of BNBT-*x*BMT thin films. As the BMT concentration increases, the (110) diffraction peaks gradually shifts to a lower diffraction angle, which implies the cell volume is expanded. Such a phenomenon may be ascribed to the substitution of the smaller ionic radius Ti<sup>4+</sup> (0.605 Å) by the larger ionic radius Mg<sup>2+</sup> (0.72 Å) [34, 35].

The surface morphologies of BNBT-*x*BMT thin films are displayed in Fig. 2a–d. Figure 2e displays the cross-sectional morphology of the BNBT-0.5BMT thin film. The surfaces of all the thin films exhibit relatively flat and crack-free microstructure, which ensures that the thin films possess favorable dielectric properties. While pinholes can be observed on all the thin film surfaces, which is caused by the volatilization of bismuth, sodium elements, and organic components at high temperatures. The cross-sectional microstructure of the BNBT-0.5BMT thin film confirms the dense structure and also shows that the thickness of BNBT-0.5BMT thin film is approximately 430 nm.

To better comprehend the influence of BMT doping upon the dielectric behavior, the dielectric constant and dielectric loss at room temperature from 100 Hz to 1 MHz versus frequency is shown in Fig. 3. As the frequency increases, the dielectric constant of each composition decreases, which stems from that the polarization cannot immediately keep up with the change in the electric field at high frequencies [36]. Moreover, the dielectric constant of BNBT-*x*BMT thin films increases along with the increase of the BMT concentration at 1 kHz. The reason for this phenomenon may be BMT doping causes the distortion of Ti–O octahedron, which leads to the increase of polarization [27]. Regarding the dielectric loss, the dielectric loss of all the BNBT-*x*BMT thin films maintains a fairly low and stable level under low frequencies (< 10<sup>5</sup> Hz). However, the dielectric loss shows a significant increment at high frequencies (> 10<sup>5</sup> Hz). The appearance of this phenomenon can be related to the L-C response generated by the stray inductance of the contact [37].

Temperature dependence of dielectric constant and dielectric loss of the BNBT-*x*BMT thin films tested at various frequencies from 1 kHz to 1 MHz are depicted in Fig. 4a–d. All of the BNBT-*x*BMT thin

**Fig. 1** **a** XRD patterns of the BNBT- $x$ BMT thin films with  $x = 0.3, 0.4, 0.5$  and  $0.6$ . **b** locally enlarged (110) diffraction peaks

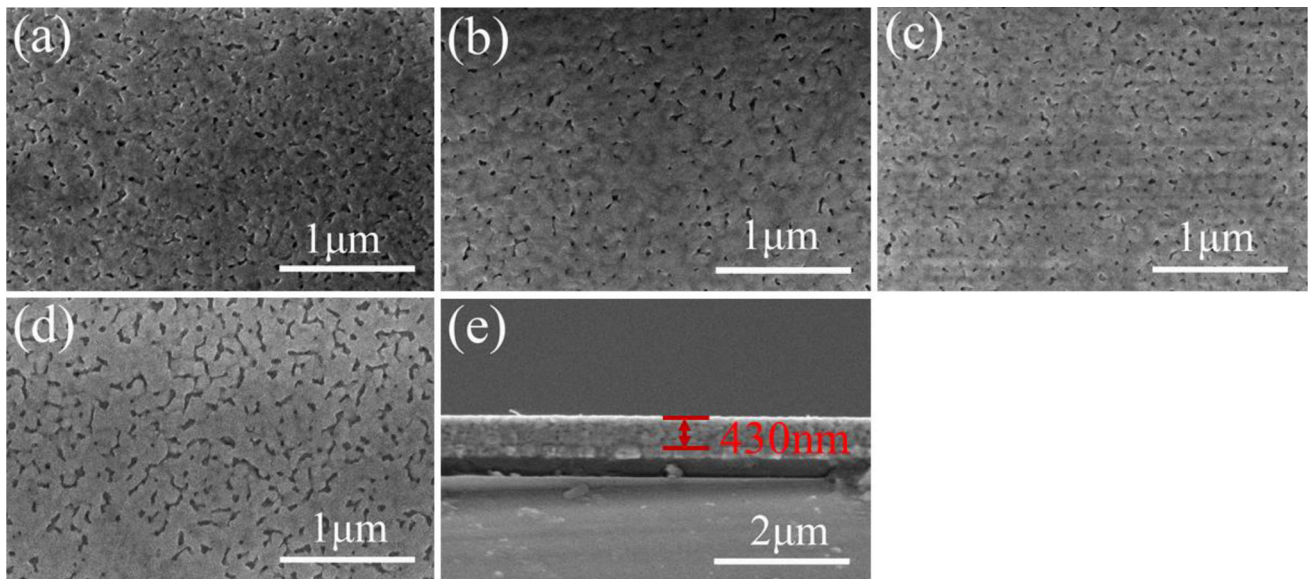
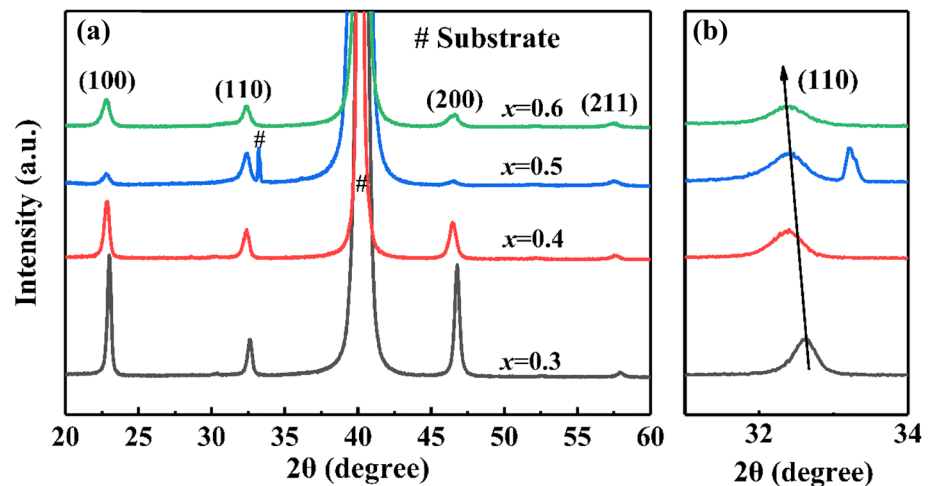


**Fig. 2** Surface morphologies of the BNBT- $x$ BMT thin films: **a**  $x = 0.3$ , **b**  $x = 0.4$ , **c**  $x = 0.5$ , **d**  $x = 0.6$ , **e** the cross-sectional micrograph of the BNBT-0.5BMT thin film

films possess a broad dielectric peak at the temperature where the dielectric constant reaches its maximum ( $T_m$ ). It is believed that a phase transition from the relaxor phase to the paraelectric phase occurs at the temperature of  $T_m$ . Zhao et al. hold the view that  $T_m$  is relevant to the emergence of tetragonal polar nanoregions (PNRs) from rhombohedral PNRs [38]. As the frequency increases, the maximum value of the dielectric constant ( $\epsilon_m$ ) gradually moves to higher temperatures, which implies the existence of nano-sized ferroelectric regions [15]. BNBT- $x$ BMT thin films maintain relatively stable and low dielectric loss ( $< 0.25$ ) at low temperatures ( $< 200$  °C), but the dielectric loss increases rapidly at high temperatures

( $> 200$  °C). This phenomenon is more severe at low frequencies. Dielectric loss at low frequencies is mainly caused by ionic conductivity. To keep the charge neutral, more oxygen vacancies are generated in the thin films to balance the  $Mg_{Ti}''$  defects, which leads to high dielectric loss. Similar behavior can be also observed in the  $Bi(Mg_{1/2}Ti_{1/2})O_3$  modified  $(Na_{1/2}Bi_{1/2})_{0.92}Ba_{0.08}TiO_3$  ceramics [39].

Due to the typical relaxor behavior of the BNBT- $x$ BMT ( $x = 0.3, 0.4, 0.5$ , and  $0.6$ ) thin films, the relaxor behavior can be analyzed according to the modified Curie–Weiss law [40]:

$$\frac{1}{\epsilon_r} - \frac{1}{\epsilon_m} = \frac{(T - T_m)^\gamma}{C} \tag{4}$$

where  $C$  is the Curie constant,  $\epsilon_r$  and  $\epsilon_m$  are dielectric constant corresponding to the temperature  $T$  and  $T_m$ , respectively.  $\gamma$  represents the degree of diffuseness, which value is between 1 and 2. If  $\gamma = 1$ , it manifests that the material is normal ferroelectrics, whereas,  $\gamma = 2$  indicates ideal relaxor ferroelectrics. Values of  $\gamma$  are obtained from the slope of the fitted

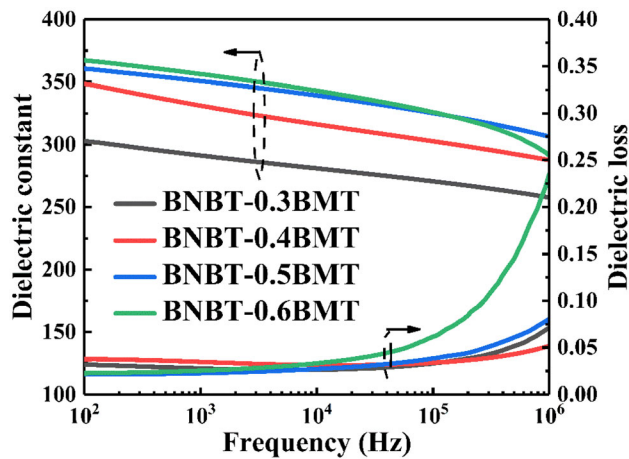


**Fig. 3** Frequency dependences the dielectric constant and dielectric loss of the BNBT- $x$ BMT thin films

curves displayed in Fig. 4e. The  $\gamma$  values of all components are close to 2, indicating a strong relaxor behavior of the BMT-doped thin films. Moreover, the  $\gamma$  value first increases and then decreases with the increment of BMT content, reaching a maximum value of 1.97 in BNBT-0.5BMT thin films. By reason of the inhomogeneities of size and charge differences around the substituting ions, which gives rise to the distortion of local structure and thereby leading to the generation of the local random electric field [41, 42]. The presence of local random electric fields disrupts the long-range dipole order and gives rise to the formation of PNRs, enabling the structural evolution from the ferroelectric phase to the relaxor phase [43]. In BNBT-based solid solution thin films,  $\text{Bi}^{3+}$  and  $\text{Mg}^{2+}$  are introduced into A-site and B-site of perovskite structure respectively, inevitably disturbing the local random electric field and resulting in the formation of PNRs.

The obtained piezoelectric response phase images of the BNBT thin film and the BNBT-0.5 BMT thin film are demonstrated in Fig. 5a, b, respectively. The bright and dark regions in the piezoelectric response phase image represent the randomly distributed downward and upward polarized regions in the thin films. There are long-range ordered ferroelectric domains in the BNBT thin film. When BMT is added

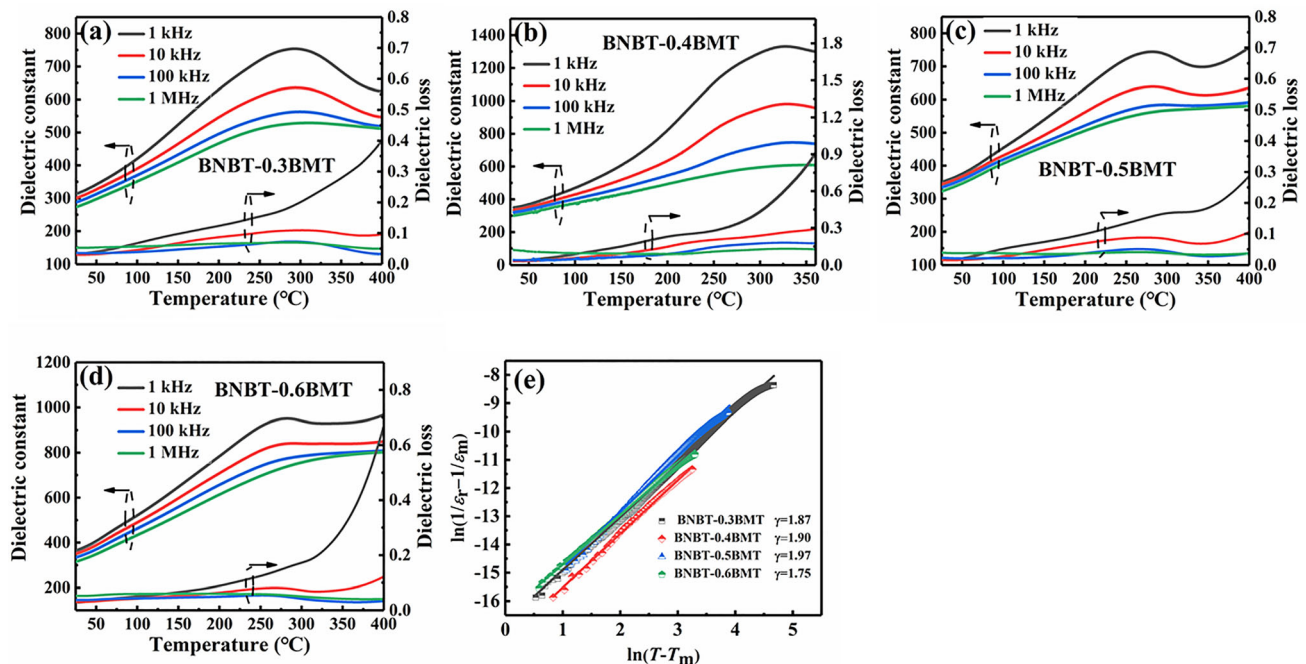


**Fig. 4** Temperature-dependent dielectric constant and dielectric loss of the BNBT- $x$ BMT thin films: **a** BNBT-0.3BMT, **b** BNBT-0.4BMT, **c** BNBT-0.5BMT, **d** BNBT-0.6BMT and **e**  $\ln(1/\epsilon_r - 1/\epsilon_m)$  versus  $\ln(T - T_m)$  of BNBT-0.5BMT thin film

into BNBT thin films, the domains become smaller and less regular, indicating the presence of PNRs [41]. Besides, it is hard to observe uniform and continuous large-scale domains. It is also demonstrated that the incorporation of BMT breaks the long-range ferroelectric domains of the BNBT thin films leading to the strong relaxor behavior of the BNT-0.5BMT thin films, which is also mutually confirmed with the previous discussion.

The  $P$ - $E$  hysteresis loops of the BNBT- $x$ BMT ( $x = 0.3, 0.4, 0.5$ , and  $0.6$ ) thin films measured under  $1300 \text{ kV/cm}$  at room temperature are depicted in Fig. 6a. The corresponding value of maximum polarization ( $P_{\max}$ ), remnant polarization value ( $P_r$ ), and  $P_{\max}-P_r$  ( $\Delta P$ ) are listed in Table 1. As we can see, all the thin films with different BMT content show slim hysteresis loops, further proving that the introduction of BMT can realize the relaxor behavior of the BNT- $x$ BMT solid solutions. At the same electric field, the polarization gradually increases with the increment of BMT content from  $0.3$  to  $0.6$ . The  $P_{\max}$  of BNBT- $x$ BMT thin films with  $x = 0.3, 0.4, 0.5$  and  $0.6$  is  $41.25, 49.04, 50.06$ , and  $51.67 \mu\text{C/cm}^2$ , just as the Table 1 listed. Two possible factors contribute to the improved polarization in BNBT- $x$ BMT thin films. In the first place, the ionic radius of  $\text{Mg}^{2+}$  is larger than that of  $\text{Ti}^{4+}$ , so the B-site  $\text{Mg}^{2+}$  substitution can increase the relative ionic displacement and thus improve the dipole polarizability [44]. In the second place, the substitution of  $\text{Mg}^{2+}$  causes the distortion of  $\text{TiO}_6$  octahedra, which conduces to the improvement of  $P_{\max}$  of  $\text{Bi}(\text{Mg}_{0.5}\text{Ti}_{0.5})\text{O}_3$  doped thin films [45].

What's more, the remnant polarization of the thin films increases slightly from  $6.75$  to  $8.60 \mu\text{C/cm}^2$  with the addition of BMT from  $0.3$  to  $0.6$ . It is generally believed that  $\text{Mg}^{2+}$  doping as an acceptor usually generates a part of oxygen vacancies, pinning the domain wall and resulting in the increment of residual polarization [46].

Figure 6b illustrates the leakage current density versus electric field for the BNBT- $x$ BMT thin films. For each composition, the current density shows a clear increasing trend with the growth of the electric field. To some extent, this behavior may be connected with the more free oxygen vacancies released by the  $\text{Mg}_{\text{Ti}''}-\text{V}_{\text{O}''}$  defect dipoles at a high electric field [47]. The leakage current density at  $150 \text{ kV/cm}$  first decreases as the BMT concentration increases from  $0.3$  to  $0.5$  and then increases significantly at a BMT content of  $0.6$ . Besides, the best leakage current density performance of about  $5.37 \times 10^{-6} \text{ A/cm}^2$  is obtained under  $180 \text{ kV/cm}$  at the BNBT- $0.5$ BMT component. On the one hand, proper  $\text{Mg}^{2+}$  substitution for  $\text{Ti}^{4+}$  can generate defect sites and deepen the electron trap level, thus reducing the leakage current density of the thin films. On the other hand,  $\text{Mg}_{\text{Ti}''}-\text{V}_{\text{O}''}$  defect dipoles can also be formed, leading to a decrease in the concentration of free oxygen vacancies [26, 29, 48]. However, the excessive oxygen vacancies induced by  $\text{Mg}^{2+}$  doping may be released driven by the electric field, which deteriorates the insulating properties of the samples. This may be the reason for the high leakage current of BNBT- $0.6$  BMT thin film.

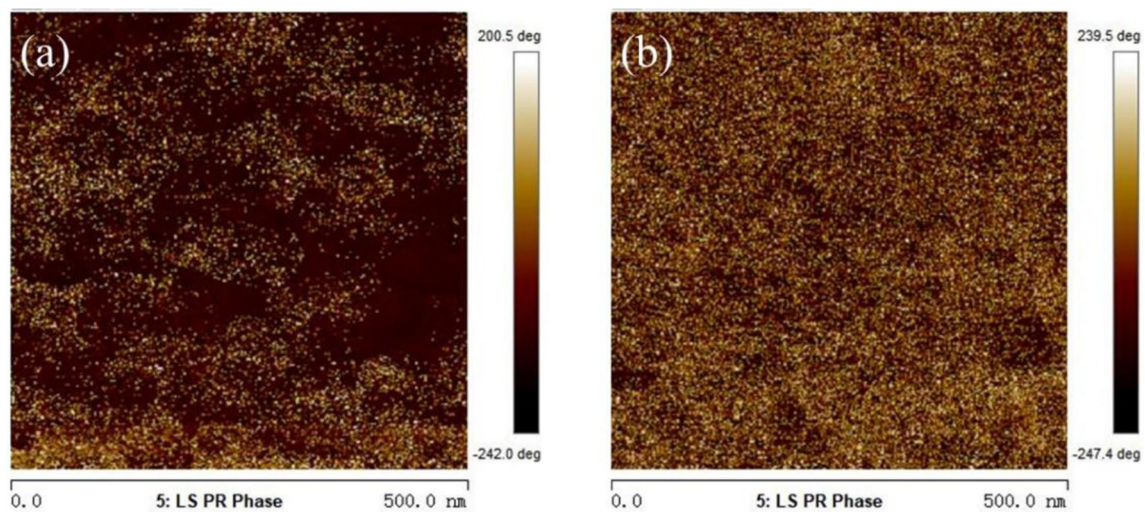


**Fig. 5** **a** PFM phase image of BNBT thin film, **b** PFM phase image of BNBT-0.5BMT thin film

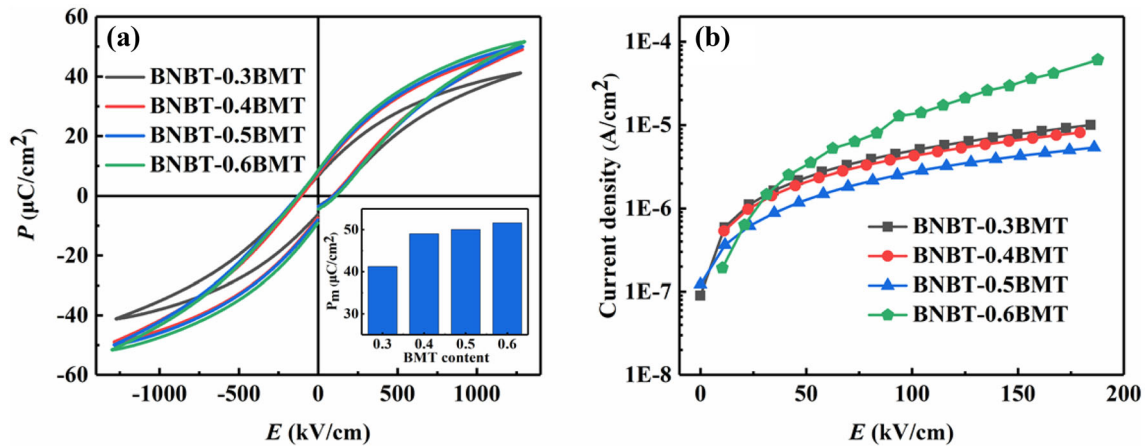


**Fig. 6** **a** The room temperature  $P$ - $E$  hysteresis loops of BNBT- $x$ BMT ( $x = 0.3, 0.4, 0.5$  and  $0.6$ ) thin films under 1300 kV/cm. The inset shows the  $P_m$  values with different BMT contents, **b** leakage current densities of BNBT- $x$ BMT thin films versus the applied electric field

**Table 1** The value of  $P_{\text{max}}$ ,  $P_r$ , and  $P_{\text{max}} - P_r$  ( $\Delta P$ ) for the BNBT- $x$ BMT thin films at 1300 kV/cm

Compositions	$P_{\text{max}}$ ( $\mu\text{C}/\text{cm}^2$ )	$P_r$ ( $\mu\text{C}/\text{cm}^2$ )	$\Delta P$ ( $\mu\text{C}/\text{cm}^2$ )
BNBT-0.3BMT	41.25	6.75	34.50
BNBT-0.4BMT	49.04	7.33	41.71
BNBT-0.5BMT	50.06	8.27	41.79
BNBT-0.6BMT	51.67	8.60	43.07

The energy storage properties of dielectric materials can be evaluated from the  $P$ - $E$  hysteresis loops. Figure 7a schematically depicts the calculation of recoverable energy storage density ( $W_{\text{rec}}$ ) and energy loss density ( $W_{\text{loss}}$ ), as shown in the green and yellow areas, respectively. Figure 7b illustrates the  $P$ - $E$  loops measured near the BDS of the BNBT- $x$ BMT thin films, and the inset of Fig. 7b depicts the breakdown strength of each composition. As discussed above, appropriate BMT doping can enhance the polarization of BNBT- $x$ BMT thin films, which is more obvious at a high electric field and the maximum polarization value of  $66.02 \mu\text{C}/\text{cm}^2$  was achieved in BNBT-0.5BMT thin film. In a word, the optimal breakdown and polarization properties were obtained in BNBT-0.5BMT thin film, which is crucial for the improvement of  $W_{\text{rec}}$ . The  $W_{\text{rec}}$  and energy storage efficiency ( $\eta$ ) as a function of the electric field of BNBT- $x$ BMT thin films are depicted in Fig. 7c and d, respectively. As is desired, the  $W_{\text{rec}}$  values of all samples increase almost linearly with the increase of the electric field. However, the value of  $\eta$  shows the opposite trend, which is on account of the higher  $W_{\text{loss}}$  at a high

electric field. The  $W_{\text{rec}}$  values of the thin films are improved slightly with the addition of  $\text{Bi}(\text{Mg}_{0.5}\text{Ti}_{0.5})\text{O}_3$  under a low electric field, which may be related to the increase of polarization. While, with the further increase of BMT concentration, the breakdown field strength of BNBT-0.6BMT thin film drops, hence the  $W_{\text{rec}}$  is greatly significantly reduced. All in all, because of the improvement of polarization and breakdown strength, an optimal  $W_{\text{rec}}$  of  $34.36 \text{ J}/\text{cm}^3$  and the  $\eta$  of 56.63% were obtained in BNBT-0.5BMT thin film at a relatively high field strength of 2149 kV/cm.

Frequency stability, thermal stability, and fatigue durability are crucial properties that guarantee the thin film capacitors operating well in severe conditions. Figure 8a illustrates the room temperature  $P$ - $E$  loops of the BNBT-0.5BMT thin film under 1200 kV/cm at various frequencies, and the corresponding  $W_{\text{rec}}$  and  $\eta$  versus frequency are shown in Fig. 8b. The bipolar  $P$ - $E$  loops maintain a slender and stable shape with the increase of frequency from 500 Hz to 5 kHz. The  $W_{\text{rec}}$  of BNBT-0.5BMT thin film varies slightly from 17.90 to  $17.74 \text{ J}/\text{cm}^3$  and the  $\eta$  increases from 65.57 to 67.73%, indicating high-frequency stability. Apart from frequency stability, the  $P$ - $E$  loops of BNBT-0.5BMT thin film measured in the temperature range from 30 °C to high temperature of 145 °C are shown in Fig. 8c and the corresponding  $W_{\text{rec}}$  and  $\eta$  are summarized in Fig. 8d. It reveals that the slender  $P$ - $E$  loops do not undergo any particular change in shape when the temperature increases from 30 to 145 °C. And the value of  $P_{\text{max}}$  only increases from  $54.26 \mu\text{C}/\text{cm}^2$  to  $57.67 \mu\text{C}/\text{cm}^2$ , which

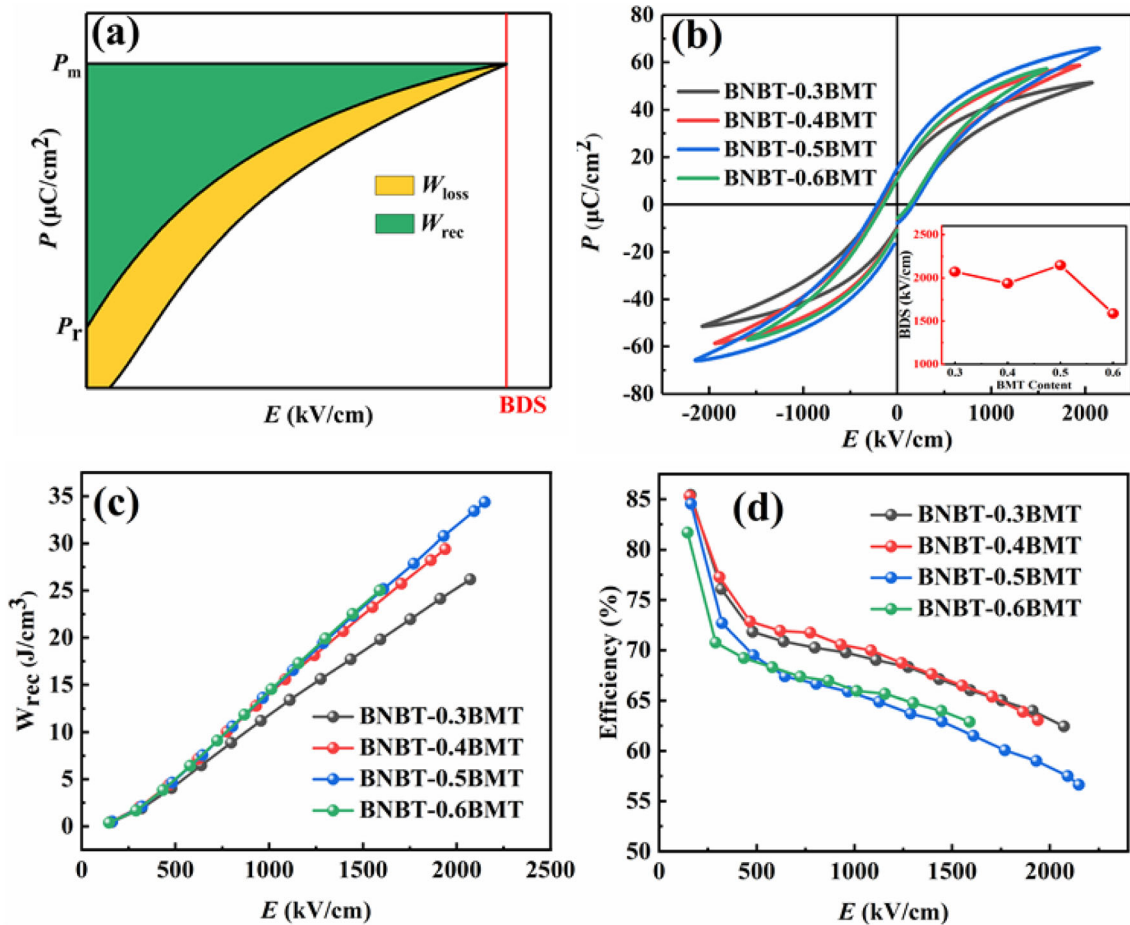


**Fig. 7** **a** Schematic diagram of energy storage for BNBT- $x$ BMT thin films. **b**  $P$ - $E$  loops of BNBT- $x$ BMT thin films measured near their breakdown strength. The inset shows their corresponding

breakdown strength values. **c** The recoverable energy density ( $W_{\text{rec}}$ ) and **d** energy conversion efficiency ( $\eta$ ) of all the samples under different electric fields

is due to the increase in temperature provides extra energy for promoting domain switching [49]. The corresponding  $W_{\text{rec}}$  decreases from 18.32 to 17.33 J/cm<sup>3</sup> and  $\eta$  decreases from 65.99 to 58.96%, which manifesting the excellent thermal stability of BNBT-0.5BMT thin film capacitor. Therefore, excellent thermal stability makes it possible for thin film capacitors to work under severe high temperatures, such as hybrid electric vehicles ( $\sim 140$  °C) [50]. Finally, long-term durability is significant for practical applications. Therefore, the fatigue test was conducted to evaluate the fatigue durability of the capacitor. Figure 8e gives the room temperature  $P$ - $E$  loops of the BNBT-0.5BMT thin film under different switching cycles. The obtained  $W_{\text{rec}}$  and  $\eta$  are shown in Fig. 8f. Surprisingly, it is hard to distinguish the  $P$ - $E$  loop from the original one in shape after 1000 cycles. And the fluctuations of both  $W_{\text{rec}}$  and  $\eta$  are

less than 3% after 10<sup>5</sup> cycling and little deterioration reveals the good anti-fatigue property of the thin film. Excellent frequency, thermal and fatigue endurance stability further prove that BNBT-0.5BMT thin film is a commendable material for energy storage applications.

## 4 Conclusions

In conclusion, lead-free BNBT- $x$ BMT ( $x = 0.3, 0.4, 0.5$  and  $0.6$ ) thin films were successfully prepared on Pt/Ti/SiO<sub>2</sub>/Si substrates by sol-gel method. The incorporation of BMT enhanced the relaxor behavior and improved the polarization of the BNBT- $x$ BMT films. In addition, proper BMT doping also reduced the leakage current density and improved the breakdown strength of the thin films. A high recoverable energy density of 34.36 J/cm<sup>3</sup> and an energy



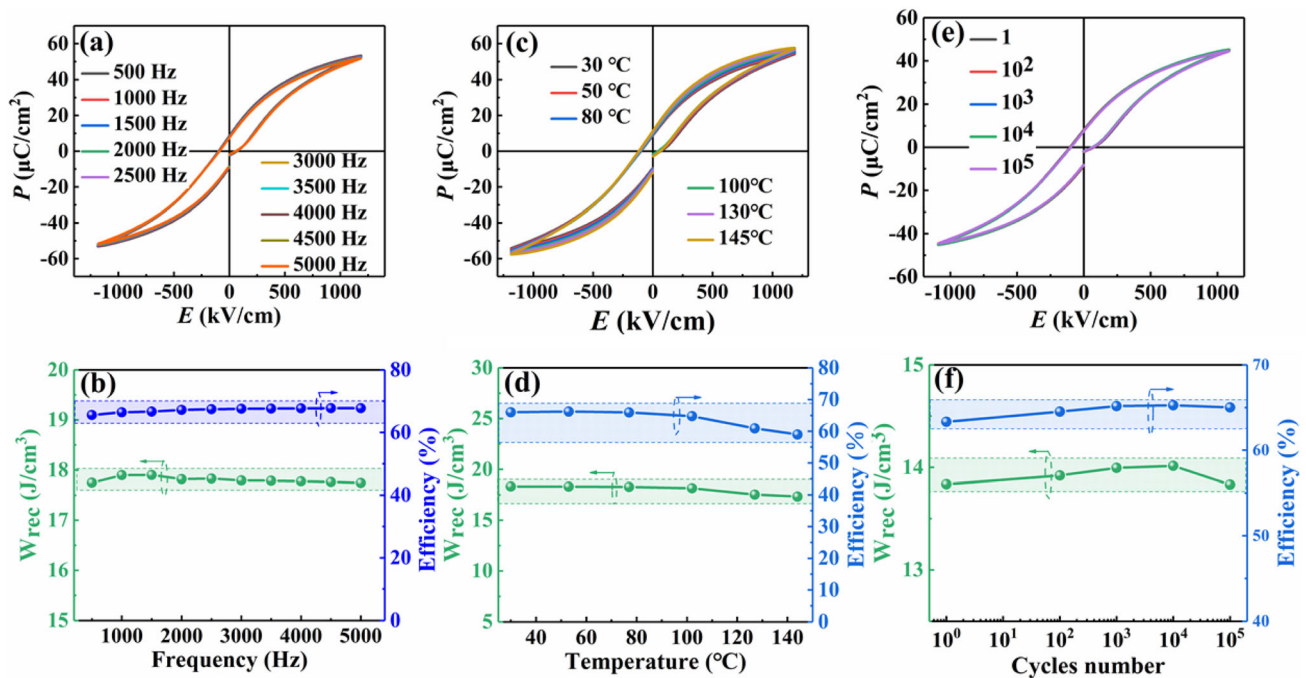


**Fig. 8** **a** Frequency-dependent  $P$ – $E$  loops of BNBT-0.5BMT thin film at 1200 kV/cm. **b** the corresponding  $W_{rec}$  and  $\eta$  at different frequencies. **c** Temperature-dependent  $P$ – $E$  loops of BNBT-0.5BMT thin film under 1200 kV/cm. **d** the corresponding  $W_{rec}$

and  $\eta$  at different temperatures. **e**  $P$ – $E$  loops of BNBT-0.5BMT thin film after different fatigue cycles under 1100 kV/cm. **f** the corresponding  $W_{rec}$  and  $\eta$  after different fatigue cycles

efficiency of 56.63% were simultaneously obtained in the BNBT-0.5BMT thin film under the electric field of 2149 kV/cm. More importantly, the BNBT-0.5BMT thin film maintained stable energy storage performance in the temperature range of 30 °C–145 °C, the frequency range of 500 Hz–5 kHz, and after  $1 \times 10^5$  fatigue cycles. All these advantages demonstrate that the BNBT-0.5BMT thin film is an alternative material for applications in electrostatic capacitors and embedded devices.

### Acknowledgements

This work was supported by National Natural Science Foundation of China (Nos. 51332003, and 51372171).

### Declarations

**Conflict of interest** All authors declare that they have no conflict of interest.

### References

1. X. Hao, J. Adv. Dielect. **3**, 1330001 (2013)
2. J. Gao, Y. Wang, Y. Liu, X. Hu, X. Ke, L. Zhong, Y. He, X. Ren, Sci. Rep. **7**, 1–10 (2017)
3. M. Braga, J. Oliveira, A. Murchison, J. Goodenough, Appl. Phys. Rev. **7**, 011406 (2020)
4. T.M. Correia, M. McMillen, M.K. Rokosz, P.M. Weaver, J.M. Gregg, G. Viola, M.G. Cain, J. Am. Ceram. Soc. **96**, 2699–2702 (2013)
5. J. Li, F. Li, Z. Xu, S. Zhang, Adv. Mater. **30**, 1802155 (2018)
6. T. Shao, H. Du, H. Ma, S. Qu, J. Wang, J. Wang, X. Wei, Z. Xu, J. Mater. Chem. A **5**, 554–563 (2017)
7. L. Yang, X. Kong, F. Li, H. Hao, Z. Cheng, H. Liu, J.-F. Li, S. Zhang, Prog. Mater. Sci. **102**, 72–108 (2019)
8. W. Sarjeant, I.W. Clelland, R.A. Price, Price Proc. IEEE **89**, 846–855 (2001)
9. Z. Liang, M. Liu, C. Ma, L. Shen, L. Lu, C.-L. Jia, J. Mater. Chem. A **6**, 12291–12297 (2018)
10. Y. Qiao, X. Yin, T. Zhu, H. Li, C. Tang, Prog. Polym. Sci. **80**, 153–162 (2018)
11. Q. Li, F.-Z. Yao, Y. Liu, G. Zhang, H. Wang, Q. Wang, Annu. Rev. Mater. Res. **48**, 219–243 (2018)
12. L. Sun, Z. Shi, L. Liang, S. Wei, H. Wang, D. Dastan, K. Sun, R. Fan, J. Mater. Chem. C **8**, 10257–10265 (2020)

13. L. Sun, Z. Shi, H. Wang, K. Zhang, D. Dastan, K. Sun, R. Fan, *J. Mater. Chem. A* **8**, 5750–5757 (2020)
14. C. Yang, J. Qian, Y. Han, P. Lv, S. Huang, X. Cheng, Z. Cheng, *J. Mater. Chem. A* **7**, 22366–22376 (2019)
15. C. Yang, P. Lv, J. Qian, Y. Han, J. Ouyang, X. Lin, S. Huang, Z. Cheng, *Adv. Energy Mater.* **9**, 1803949 (2019)
16. K. Yao, S. Chen, M. Rahimabady, M.S. Mirshekarloo, S. Yu, F.E.H. Tay, T. Sritharan, L. Lu, *IEEE Trans. Sonics Ultrason.* **58**, 1968–1974 (2011)
17. H. Palneedi, M. Peddigari, G.T. Hwang, D.Y. Jeong, J. Ryu, *Adv. Funct. Mater.* **28**, 1803665 (2018)
18. X. Kong, L. Yang, Z. Cheng, S. Zhang, *Materials* **13**, 180 (2020)
19. P. Chen, S. Wu, P. Li, J. Zhai, B. Shen, *Ceram. Int.* **44**, 6402–6408 (2018)
20. Z. Zhou, J. Luo, W. Sun, J.-F. Li, *Phys. Chem. Chem. Phys.* **19**, 19992–19997 (2017)
21. T.H. Dinh, H.-S. Han, J.-S. Lee, C.-W. Ahn, I.-W. Kim, M.R. Bafandeh, *J. Korean Phys. Soc.* **66**, 1077–1081 (2015)
22. J.-H. Cho, J.-S. Park, S.-W. Kim, Y.-H. Jeong, J.-S. Yun, W.-I. Park, Y.-W. Hong, J.-H. Paik, *J. Eur. Ceram. Soc.* **37**, 3313–3318 (2017)
23. H. Qi, R. Zuo, *J. Mater. Chem. A* **7**, 3971–3978 (2019)
24. W. Huang, S.K. Thatikonda, Y. Ke, X. Du, N. Qin, A. Hao, D. Bao, *J. Am. Ceram. Soc.* **103**, 999–1009 (2020)
25. D.-K. Kwon, M.H. Lee, *IEEE Trans. Sonics Ultrason.* **59**, 1894–1899 (2012)
26. P. Chen, P. Li, J. Zhai, B. Shen, F. Li, S. Wu, *Ceram. Int.* **43**, 13371–13376 (2017)
27. N. Sun, Y. Li, X. Liu, X. Hao, *J. Power Sources* **448**, 227457 (2020)
28. Y. Zhang, W. Li, Y. Qiao, Y. Zhao, Z. Wang, Y. Yu, H. Xia, Z. Li, W. Fei, *Appl. Phys. Lett.* **112**, 093902 (2018)
29. Y. Zhang, W. Li, W. Cao, Y. Feng, Y. Qiao, T. Zhang, W. Fei, *Appl. Phys. Lett.* **110**, 243901 (2017)
30. M. Budimir, D. Damjanovic, N. Setter, *Phys. Rev. B* **72**, 064107 (2005)
31. K. Shan, Z.-Z. Yi, X.-T. Yin, L. Cui, D. Dastan, H. Garmestani, F.M. Alamgir, *J. Alloys Compd.* **855**, 157465 (2021)
32. X.-T. Yin, J. Li, D. Dastan, W.-D. Zhou, H. Garmestani, F.M. Alamgir, *Sens. Actuators.* **319**, 128330 (2020)
33. Y. Guo, M. Li, W. Zhao, D. Akai, K. Sawada, M. Ishida, M. Gu, *Thin Solid Films* **517**, 2974–2978 (2009)
34. R. D. Shannon, *Acta Crystallogr. A* **32**, 751–767 (1976)
35. B. Xiong, H. Hao, S. Zhang, H. Liu, M. Cao, *J. Am. Ceram. Soc.* **94**, 3412–3417 (2011)
36. C. Yang, J. Qian, Y. Han, X. Sun, Z. Sun, L. Chen, *Ceram. Int.* **44**, 7245–7250 (2018)
37. Y. Zhang, W. Li, S. Xu, Z. Wang, Y. Zhao, J. Li, W. Fei, *J. Mater. Chem. A* **6**, 24550–24559 (2018)
38. W. Zhao, R. Zuo, J. Fu, M. Shi, *J. Eur. Ceram. Soc.* **34**, 2299–2309 (2014)
39. P. Chen, B. Chu, *J. Eur. Ceram. Soc.* **36**, 81–88 (2016)
40. J. Chen, Z. Tang, B. Yang, S. Zhao, *J. Mater. Chem. A* **8**, 8010–8019 (2020)
41. N. Sun, Y. Li, Q. Zhang, X. Hao, *J. Mater. Chem. C* **6**, 10693–10703 (2018)
42. A. Kumar, R. Kumar, K. Singh, S. Singh, *Phys. Status Solidi A* **216**, 1800786 (2019)
43. J. Chen, Z. Tang, Q. Lu, S. Zhao, *J. Alloys Compd.* **756**, 62–67 (2018)
44. Y. Wu, X. Wang, L. Li, *J. Am. Ceram. Soc.* **94**, 2518–2522 (2011)
45. E. Kan, H. Xiang, C. Lee, F. Wu, J. Yang, M.H. Whangbo, *Angew. Chem.* **122**, 1647–1650 (2010)
46. P. Li, W. Li, J. Zhai, B. Shen, H. Zeng, K. Zhao, *RSC Adv.* **5**, 62713–62718 (2015)
47. Y. Han, Y. Wang, C. Yang, Q. Yao, J. Chen, S. Huang, *Ceram. Int.* **44**, 15153–15159 (2018)
48. J. Wang, Y. Li, N. Sun, J. Du, Q. Zhang, X. Hao, *J. Eur. Ceram. Soc.* **39**, 255–263 (2019)
49. C. Yang, Y. Han, C. Feng, X. Lin, S. Huang, X. Cheng, Z. Cheng, *A.C.S. Appl. Mater. Interfaces* **12**, 6082–6089 (2020)
50. C. Yang, J. Qian, P. Lv, H. Wu, X. Lin, K. Wang, J. Ouyang, S. Huang, X. Cheng, Z. Cheng, *Journal of Materiomics* **6**, 200–208 (2020)

**Publisher's Note** Springer Nature remains neutral with regard to jurisdictional claims in published maps and institutional affiliations.